JGR Oceans

RESEARCH ARTICLE
10.1029/2018JC014454

High-Resolution Observations of Subsurface Fronts and Alongshore Bottom Temperature Variability Over the Inner Shelf

Thomas P. Connolly[1] **and Anthony R. Kirincich**[2]

[1]Moss Landing Marine Laboratories, Moss Landing, CA, USA, [2]Department of Physical Oceanography, Woods Hole Oceanographic Institution, Woods Hole, MA, USA

Key Points:
- Subsurface fronts are generated by the interaction of tides, stratification, and shallow bathymetry
- Fiber-optic bottom temperature sensing detects propagation of subsurface fronts
- Characteristics of high-frequency temperature variability vary dramatically over short alongshore scales

Correspondence to:
T. P. Connolly,
tconnolly@mlml.calstate.edu

Citation:
Connolly, T. P., & Kirincich, A. R. (2019). High-resolution observations of subsurface fronts and alongshore bottom temperature variability over the inner shelf. *Journal of Geophysical Research: Oceans*, *124*, 593–614. https://doi.org/10.1029/2018JC014454

Received 7 AUG 2018
Accepted 20 DEC 2018
Accepted article online 28 DEC 2018
Published online 25 JAN 2019

Abstract Circulation patterns over the inner continental shelf can be spatially complex and highly variable in time. However, few studies have examined alongshore variability over short scales of kilometers or less. To observe inner-shelf bottom temperatures with high (5-m) horizontal resolution, a fiber-optic distributed temperature sensing system was deployed along a 5-km-long portion of the 15-m isobath within a larger-scale mooring array south of Martha's Vineyard, MA. Over the span of 4 months, variability at a range of scales was observed along the cable over time periods of less than a day. Notably, rapid cooling events propagated down the cable away from a tidal mixing front, showing that propagating fronts on the inner shelf can be generated locally near shallow bathymetric features in addition to remote offshore locations. Propagation velocities of observed fronts were influenced by background tidal currents in the alongshore component and show a weak correlation with theoretical gravity current speeds in the cross-shore component. These events provide a source of cold, dense water into the inner shelf. However, differences in the magnitude and frequency of cooling events at sites separated by a few kilometers in the alongshore direction suggest that the characteristics of small-scale variability can vary dramatically and can result in differential fluxes of water, heat, and other tracers. Thus, under stratified conditions, prolonged subsurface observations with high spatial and temporal resolution are needed to characterize the implications of three-dimensional circulation patterns on exchange, especially in regions where the coastline and isobaths are not straight.

Plain Language Summary This study examines in detail how ocean temperature varies along a 5-km stretch of coastline off of Martha's Vineyard, MA, the site of a long-term ocean observatory. In addition to the gradual changes in ocean temperature that occur over long distances of hundreds of kilometers or more along the coast, there can also be sharp fronts where temperature changes rapidly over much shorter distances. Little is known about these features because they occur below the surface, move through the ocean, and are often short lived. To learn more about small-scale fronts and how they change with time, we used traditional oceanographic sensors anchored at a few specific locations and also laid a fiber-optic cable along the ocean floor at a depth of 15 m. This fiber-optic system continuously recorded hundreds of simultaneous temperature measurements along the coastline for several months. These measurements show that small-scale fronts often occur near a shallow shoal where there are strong tidal currents. However, the fronts also travel away from the shoal, causing rapid cooling along the sea floor as they move. Because of these subsurface fronts, temperature measurements at just one location may not be representative of other nearby locations just a few kilometers away.

1. Introduction

The physical dynamics of the inner continental shelf are governed by complex interactions between stratification, rotation, and turbulent boundary layers. These interactions occur across a range of spatial scales spanning the shelf width down to the submesoscale and are modulated by forcing mechanisms with a similarly broad range of time scales, including seasonally varying air-sea heat fluxes, synoptic weather systems and tides. The role of along-shelf wind stress in driving cross-shelf exchange is diminished over the inner shelf, and it is possible that small-scale features contribute greatly to the transport of heat and tracers. However, conceptual models of inner-shelf dynamics often neglect alongshore variability at scales of kilometers

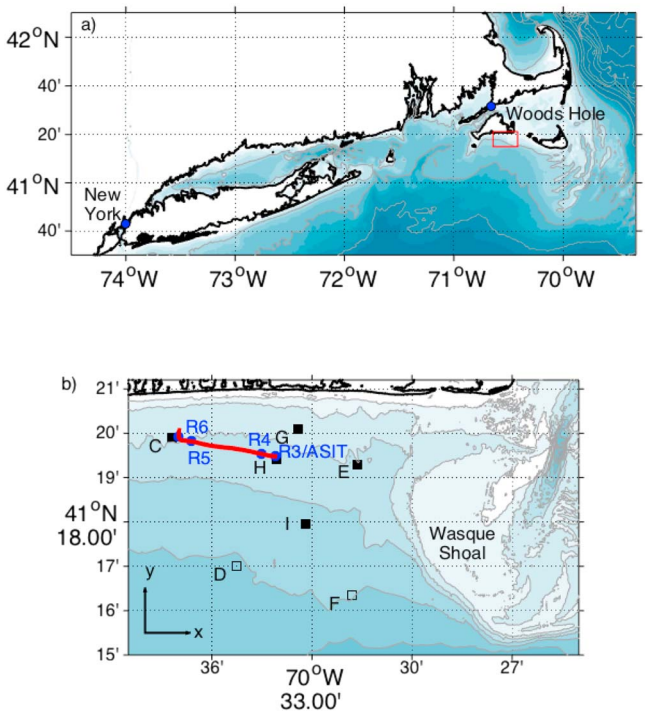

Figure 1. (a) Map of the U.S. east coast with the study area at the inner shelf south of the island of Martha's Vineyard marked in red. Gray contours indicate 20-m bottom depth increments. (b) The study area with observational components: (red line) the bottom-laid distributed temperature sensing fiber-optic cable, (blue circles) calibration points for the distributed temperature sensing system, and (black squares) the hydrographic and velocity mooring locations. The mooring-based observations used in this study are indicated with filled squares, while gray contours indicate 5-m bottom depth increments. Unfilled squares indicate contemporaneous mooring locations not used in this study (sites D and F). Coordinate system is shown in the lower left corner. ASIT = Air-Sea Interaction Tower.

or less for simplicity, and there are currently few available observations that resolve these scales, particularly below the surface (Lentz & Fewings, 2012). Over the inner shelf south of Martha's Vineyard, Massachusetts (Figure 1), three-dimensional circulation patterns can result from complex bathymetry, an irregular coastline, strong stratification, and along-shelf variability in tidal current amplitude (Kirincich & Lentz, 2017a). This study presents a unique set of high-resolution observations at the Martha's Vineyard Coastal Observatory (MVCO), which reveal differences in bottom temperature variability over alongshore distances of fewer than 5 km. These observations are used to characterize the temporal and spatial evolution of subsurface fronts over the inner shelf, including those generated locally where strong tidal currents flow over shallow shoals.

Among the physical mechanisms that drive variability at short horizontal scales, nonlinear internal waves and gravity currents stand out because they are characterized by strong fronts and rapid temporal changes in density. In shallow water, nonlinear waves of elevation can have trapped cores, which transport dense water over long distances and have dynamics similar to gravity currents or buoyancy-driven flows (Sinnett et al., 2018; Venayagamoorthy & Fringer, 2007). These nonlinear internal waves are often called *bores* in order to describe the characteristic surge of dense water at a sharp front. Internal bores in the nearshore are often generated as internal waves approach the coast from deep water, steepen, and break (Woodson, 2018). Internal bores contribute to cross-shore heat fluxes (Nam & Send, 2011), sediment resuspension (Bogucki et al., 1997), and dissolved oxygen variability (Walter et al., 2014). In the shallow kelp forest environment, the effects of irregular, rocky substrate on internal bores lead to small-scale physical and biogeochemical heterogeneity (Leary et al., 2017). However, most studies have focused on evolution of fronts in the cross-shelf direction, in which gradients tend to be strongest. There have been fewer detailed examinations of the potentially important small-scale alongshore variability associated with propagating fronts over the inner shelf, especially those generated locally in shallow water.

In addition to propagating features, mixing associated with tidal currents can drive small-scale horizontal variability over the inner shelf. In shallow water depths, turbulence can prevent the development of stratification, resulting in the formation of tidal mixing fronts, sharp horizontal gradients between shallow well-mixed locations and adjacent deeper stratified locations (Simpson & Hunter, 1974). Tidal mixing fronts are often associated with tidally rectified mean flows and the generation of internal waves (Chen & Beardsley, 1995; Loder et al., 1993). Tidal currents have a significant impact on inner-shelf mixing and circulation in two-dimensional model runs (Castelao et al., 2009), but the effects of tidal mixing fronts on three-dimensional inner-shelf circulation and potential interactions with internal bores and gravity currents are less well understood.

Attaining a clear understanding of the role of smaller-scale processes on exchange across the shallow shelf requires higher-resolution observations than what is typically available. Moorings have been used to characterize the three-dimensional inner-shelf circulation (e.g., Kirincich & Barth, 2009; Tilburg & Garvine, 2003), but the number of locations that can be observed are limited. Remote sensing using satellites and high-frequency radar have identified patterns of inner-shelf lateral variability associated with bathymetric features and instabilities (Kim, 2010; Kirincich et al., 2013; Nidzieko & Largier, 2013) but are limited to the surface. A major challenge in characterizing and assessing the importance of the three-dimensional inner-shelf circulation lies in observing the range of potentially important spatial and temporal scales beneath the surface. Few observational studies have investigated the link between tides, nearshore bathymetry, and stratification in driving three-dimensional inner-shelf circulation below the surface, where both spatial and temporally high-resolution measurements are difficult to obtain.

The goals of this study are to (1) characterize subsurface temperature variability at short alongshore scales over the inner shelf and (2) identify the physical mechanisms that drive such variability in the presence of strong tidal currents, stratification, and complex nearshore bathymetry. To achieve high horizontal resolution of subsurface temperature, a fiber-optic distributed temperature sensing (DTS) system was deployed along the seabed during a larger-scale field experiment over the Martha's Vineyard inner shelf. DTS technology provides high-resolution measurements of temperature at scales of several meters or less, over distances of kilometers (Tyler et al., 2009), complementing mooring-based profiles of velocity, temperature, salinity obtained at scales of 5 km.

Further information on the study area and broader-scale mooring observations are presented first in section 2 in order to provide motivation and context for the high-resolution DTS observations that follow. The design, calibration, and performance of the DTS system are described in section 3. The high-resolution DTS observations are then used in combination with data from the moored array to characterize small-scale alongshore variability of temperature and the propagation of temperature fronts (section 4). The dynamical processes associated with the observed alongshore variability are discussed, as well as implications for the design of future observations and modeling studies (section 5).

2. The Martha's Vineyard Inner Shelf

2.1. Background

This study focuses on subsurface temperature variability during the summer season on the Martha's Vineyard inner shelf, when strong thermal stratification is present. During this season, winds are typically directed toward the southeast, which is upwelling favorable and offshore (Lentz, 2008). In addition to vertical stratification, a cross-shelf density gradient is associated with increasing temperature, and decreasing density, toward the coast (Fewings & Lentz, 2011; Horwitz & Lentz, 2014). Seasonal mean along-shelf velocities of ~0.05–0.10 m/s are directed toward the west at this site, opposing the seasonal mean wind stress (Lentz, 2008).

Tides are an important forcing mechanism for variability in velocity, temperature, and other tracers throughout the New England continental shelf region (Figure 1), including the Martha's Vineyard inner shelf. On a regional scale, over the middle to outer shelf, the M_2 tide is the largest constituent contributing to the depth averaged currents. The M_2 current ellipses over the shelf are generally circular and clockwise, with amplitudes increasing from west to east, and phase increasing with offshore distance (Shearman & Lentz, 2004). Baroclinic tidal motions are generated at the shelf break, forming nonlinear internal waves as the internal tide steepens over the shelf (Colosi et al., 2001; MacKinnon & Gregg, 2003a, 2003b; Shearman & Lentz, 2004). Offshore of the 25-m isobath, sea surface temperature fluctuations with shorter spatial scales of ~100 m have been attributed to internal waves (Farrar et al., 2007).

At shallower depths, adjacent to the MVCO, there is significant small-scale horizontal variability in the magnitude, orientation, and phase of tidal current ellipses. High-frequency radar observations show that tidal current ellipses become more circular from west to east, and amplitudes increase from ~0.15 to ~0.40 m/s (Kirincich et al., 2013). Currents near Wasque Shoal (Figure 1b) lead those off the central portion of the island by ~2 hr.

The transitions in magnitude, phase, and ellipticity of the tidal currents strongly influence the physical dynamics of the Martha's Vineyard inner shelf. Model results indicate the presence of a tidal mixing front near Wasque Shoal during the summer (Wilkin, 2006). Tidal rectification contributes to a cyclonic mean flow at the eastern end of the island (Ganju et al., 2011; Kirincich et al., 2013) Observations show that the complex bathymetry of the region significantly affects the alongshore structure of mean and eddy heat fluxes (Kirincich et al., 2013; Kirincich & Lentz, 2017a). However, despite long-term observational efforts in this region, subsurface observations have been limited in the range of spatial scales that could be resolved.

2.2. Mooring Array

The deployment of the DTS system (described in section 3) was designed to supplement a larger-scale mooring array deployed 9 June 2014 to 15 January 2015 as part of the Inner Shelf Lateral Exchange (ISLE) program (Figure 1). The moored observations are described in detail by Kirincich and Lentz (2017a). The ISLE observations used in this study are summarized in Table 1. Velocity measurements were obtained from 1,200-kHz RDI Workhorse acoustic Doppler current profilers (ADCPs) at sites C and G, from 1,000-kHz 5-beam Nortek

Table 1
Summary of Moored Temperature and Velocity Measurements

Mooring site	Water depth (m)	Variable	Measurement depths
C	15	Temperature	1, 3, 6, 9, 11 m, bottom
		Velocity	2–14 m (0.5 m)
E	15	Temperature	1, 3, 6, 9, 11, 12.8, 13.6, 14.8 m
		Velocity	0.6–10.6 m (0.5 m)
G	12	Temperature	1, 3, 6, 9 m
		Velocity	1.9–10.9 m (0.5 m)
H	16	Temperature	1, 3, 6, 9, 11 m, bottom
		Velocity	1.9–14.1 m (0.2 m)
I	22	Temperature	1, 3, 6, 9, 12, 17 m, bottom
		Velocity	1.9–19.9 m (0.5 m)

AD2CP profilers at sites E and H and a 600-kHz RDI Workhorse ADCP at site I. Moored temperature measurements were obtained using SBE-37 Microcat sensors (Seabird Electronics, nominal accuracy ±0.002 °C). Bottom temperature at site C was obtained from a SBE-26 Seagauge pressure sensor (nominal accuracy +/- 0.01 °C). Bottom temperature at site I was obtained from the ADCP (nominal precision ±0.4 °C). Additional temperature measurements collected specifically to calibrate the DTS system are described in section 3.

2.3. Mooring-Based Subsurface Variability

The ISLE moored observations provide an initial comparison of variability in water column properties across the study area. Rapid temporal changes are emphasized by analyzing time derivatives of bottom temperature, $\partial T/\partial t$. Time series of $\partial T/\partial t$ estimated from 30-min (three-point) running averages show clear differences in high-frequency variability between sites C and H, which are separated by an alongshore distance of <5 km (Figures 2a and 2b). Larger fluctuations in $\partial T/\partial t$ occur at site H, farther to the east (Figure 2a). Running 2-day standard deviations of $\partial T/\partial t$ show fluctuations in high-frequency variance at time scales of 1–2 weeks and reduced variability in August at site H (Figure 2b). A correlation analysis, using effective degrees of freedom (EDOFs; Emery & Thomson, 2004), shows that the running standard deviations of $\partial T/\partial t$ are significantly correlated between sites H and E ($r = 0.76, p = 0.010, EDOF = 8$). High-frequency bottom temperature variability is almost always elevated toward the east, highest at site E and lowest at site C.

Background thermal stratification, as indicated by the 2-day running mean of the vertical temperature gradient $\partial T/\partial z$, is similar at sites C, H, and E (Figure 2c). Large, correlated fluctuations occur on time scales of 7–10 days, similar time scales as the running standard deviation of $\partial T/\partial t$ (Figures 2b and 2c). These two quantities are weakly but significantly correlated, both at site H ($r = 0.60, p = 0.014, EDOF = 14$) and at site E ($r = 0.75, p = 0.001, EDOF = 12$).

In addition to background stratification, tidal currents are another potential factor determining high-frequency temperature variability. Temporal fluctuations in high-frequency velocity variance were estimated using a 2-day running standard deviation of alongshore velocity 2 m above the seabed at site C (Figure 2d, solid line). The high-frequency velocity variance at this site varies between ~0.08 and 0.10 m/s over a time scale of approximately one month. At site E (not shown), the high-frequency velocity variance fluctuates with similar timing but greater magnitudes of 0.15–0.21 m/s, consistent with the results of Kirincich et al. (2013), which show stronger tidal currents to the east near Wasque Shoal. A harmonic fit of the bottom velocity (Pawlowicz et al., 2002), using only the M_2, S_2, and N_2 frequencies, shows that a combination of semidiurnal components can explain the magnitude and timing of this monthly cycle at site C (Figure 2d, dashed line). This monthly cycle is not evident in $\partial T/\partial t$ or in estimates of the vertical stratification present at the mooring sites, estimated via the top to bottom temperature gradient (Figure 2b). The timing of high-frequency bottom temperature variability at site H therefore appears to be more related to the strength of background stratification than the strength of tidal forcing.

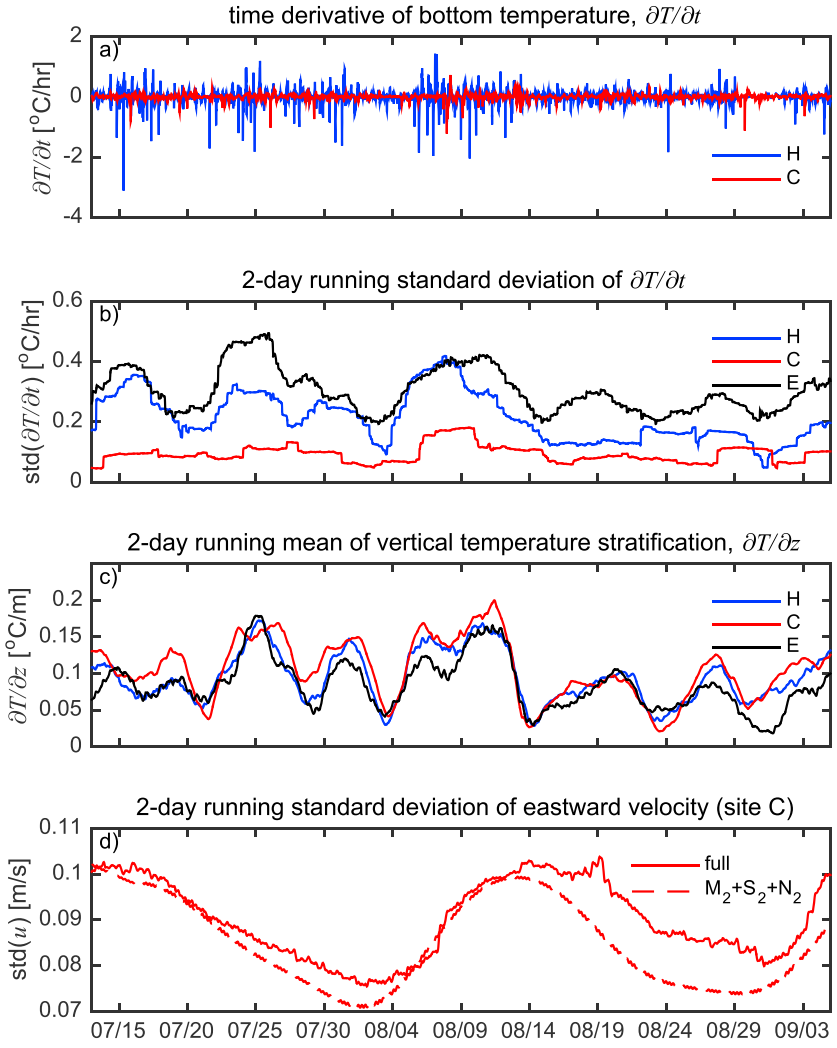

Figure 2. High-frequency bottom temperature variability, stratification, and velocity variability. (a) Time derivative of bottom temperature, $\partial T/\partial t$, at sites H (blue) and C (red). Note that site E is not shown in this panel for clarity. (b) Two-day running standard deviation of $\partial T/\partial t$ at sites H, C, and E. Higher values indicate relatively strong high-frequency temperature variability. (c) Two-day running mean of top to bottom temperature stratification at sites H, C, and E. (d) Two-day running standard deviation of near-bottom velocity, 2 m above the seabed, at site C. Solid line indicates results using the full velocity signal; dashed line indicates results using only the M_2, S_2, and N_2 semidiurnal tidal harmonics. Higher values indicate relatively strong tidal currents.

Based solely on these moored observations, subsurface temperature variability over the inner shelf off Martha's Vineyard can be characterized by variability over days to weeks, as well as shorter period fluctuations at tidal time scales. However, neither the driver of the subsurface temperature variability nor the cause of the sizable differences between sites H and C can be explained based on the mooring data alone. Thus, additional high-resolution observations are needed to understand the processes that influence high-frequency temperature variability at time scales of 2 days or less and their implications on inner-shelf circulation.

3. DTS System

3.1. Setup and Deployment

To investigate the processes that drive small-scale alongshore variability over the inner shelf in detail, a DTS system was deployed at the MVCO during the period 11 July to 31 October 2014. DTS systems consist of a laser-based sampling instrument connected to one or more fiber-optic cables that are used to sample the

environmental temperature. At the MVCO Air-Sea Interaction Tower (ASIT), a fixed structure that extends from the seabed above the air-sea interface, two 5-km-long fiber-optic cables were deployed approximately along the 15-m isobath (Figure 1b). One cable was deployed extending westward from the ASIT at the seabed, between ISLE mooring sites H and C. Near site C, a 515-m segment of the cable is oriented onshore. A second cable (not shown) was deployed to the east of ASIT, extending past site E, but was dragged and snapped by a trawler soon after deployment. Heavy trawling activity also precluded the deployment of a cable in the cross-shore direction, extending offshore of ASIT. On the ASIT, an XT-DTS^{TM} (Silixa Ltd., Elstree, Hertfordshire, UK) instrument was used to sample 1-m intervals along the cable, for a duration of 30 s every minute. The instrument was connected to a node on the ASIT platform, which provided power and ethernet communication from shore.

The cable, a Mini LT Flat Drop cable from Optical Fiber Solutions, is approximately 4 × 8 mm wide and contains internal strength members that support a channel with two fibers between them. Deployed starting at the ASIT end, the portion of the cable to be connected to the DTS instrument on ASIT was secured to an anchor, which was lowered from the ship to the seabed near the base of the tower. Strain relief was installed on the anchor to minimize tension on the cable. The remaining cable was then spooled off the ship as it moved away from ASIT. The cable is negatively buoyant, but additional weights (~0.5 kg) were attached periodically to ensure a fixed position on the seabed. After finishing this part of the deployment 4.9 km away from the ASIT, divers retrieved the remaining portion from the anchor near ASIT and ran it up to the ASIT platform, where the DTS instrument and a calibration bath were installed. A 22-m coil remained on the anchor for calibration purposes (section 3.2). The portion of the cable exposed to the air-sea interface was protected with plastic tubing installed before deployment and secured to the leg of the tower. No change in the position of the cable was evident upon recovery.

3.2. DTS Calibration

The DTS measurement is based on Raman scattering of light, which is dependent on temperature. A brief summary of the relevant theory and its application to DTS is provided in Appendix A. The DTS instrument emits a laser pulse down the fiber optic cable, and optical receivers measure the intensity of Stokes and anti-Stokes backscatter, which correspond to lower and higher frequencies, respectively. The ratio of measured backscatter intensities is a function of temperature

$$T(d) = \frac{\gamma}{\ln \frac{P_s(d)}{P_{as}(d)} + C - \Delta\alpha d}, \tag{1}$$

where T (K) is temperature, d (m) is distance along the cable, P_s/P_{as} is the ratio of observed Stokes and anti-Stokes backscatter intensities, and the parameters $\Delta\alpha$ (m^{-1}), C, and γ (K) are determined through calibration (Hausner et al., 2011). Physical meanings of these calibration parameters are discussed in Appendix A.

In the present study, a total of five independent temperature sensors are used to calibrate the DTS system and evaluate the temperature error (Figure 1b). On the tower platform above the air-sea interface, 43 m of the cable was placed in a water-filled cooler with an SBE-39 temperature sensor sampling at 30-s intervals with nominal initial accuracy ±0.002 °C. At the base of ASIT near the seabed (site R3, Figure 1b), an SBE-39 sensor was colocated with 22-m coil of cable. This sensor also provided the bottom temperature time series for mooring site H. In addition, three Water Temp Pro (Onset Computer Corporation, Bourne, MA) temperature loggers were attached to the cable at estimated distances 925, 3,945, and 4,575 m from the instrument (sites R4, R5, and R6, Figure 1b). These sensors have accuracy of ~ 0.1°C (Lentz et al., 2013) and were programmed to sample every 10 min. The DTS data were averaged in segments of 5-m length and 10-min time in order to decrease noise and make temporal resolution consistent with the calibration data.

With a total of five independent temperature measurements along the distance of the cable, it is possible to calibrate the cable temperature at three locations and evaluate the error at two other locations. In order to constrain equation (1), it is necessary to have calibration sections measuring at least two different temperatures and also have a long separation between at least two of the sensors. To maximize temperature differences, distances between points and sensor accuracy, calibration was performed using the cooler on ASIT, R3, and R6. Because the calibration coefficients vary with operating conditions, best results are obtained when a dynamic calibration is performed for each time (Hausner et al., 2011).

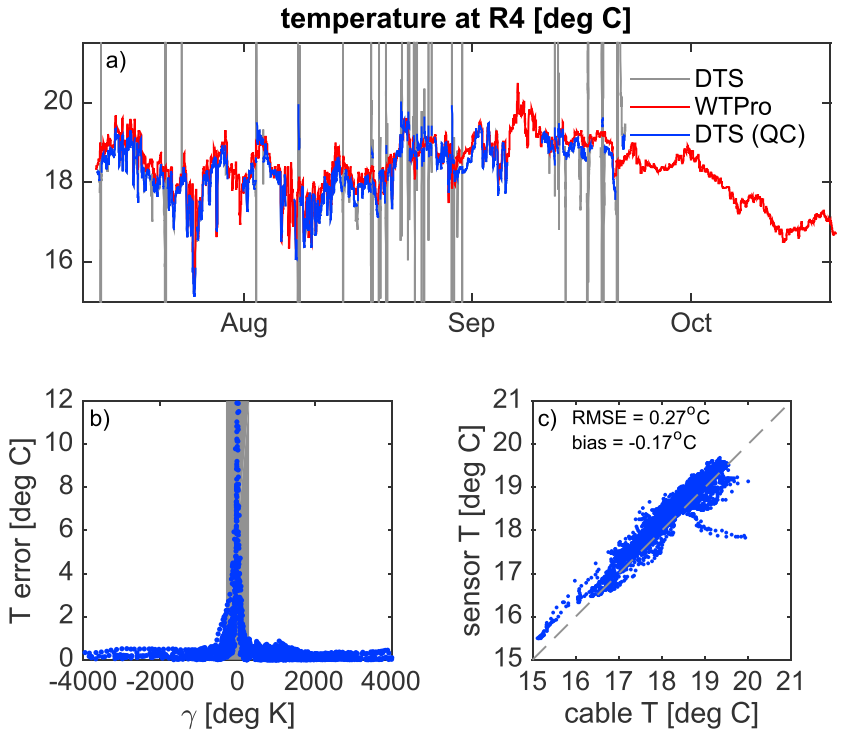

Figure 3. Summary of results from calibration section R4. (a) Temperature from the DTS system with no quality control (gray), the WaterTemp Pro sensor (WTPro, red), and quality-controlled data from the DTS system (blue). The DTS temperature in this figure is derived from a three-point calibration at Air-Sea Interaction Tower, R3, and R6. (b) Dependence of DTS error on calibration parameter γ. Gray shading indicates the range $|\gamma| < 300$ K used as a quality control threshold to exclude time periods with large errors from analysis. (c) Quality-controlled DTS data versus sensor data. DTS = distributed temperature sensing; RMSE = root-mean-square error.

3.3. Evaluation of DTS Measurements

A quality control procedure was implemented to remove times when temperatures at the calibration points are similar and calibration parameters are unconstrained. Large errors occur when the parameter γ falls within a narrow range (Figure 3b). A quality control threshold in which DTS data are flagged as bad if $|\gamma| < 300$ K removes the largest errors (Figures 3a and 3b). The calibration parameters γ and C are highly correlated ($R^2 > 0.99$) so a threshold based on C would work equally as well. Although the largest errors also occur within a narrow range of $\Delta\alpha$ values, a threshold based on $\Delta\alpha$ would also eliminate many points with low error values (not shown). The quality-controlled data at R4 have a root-mean-square error (RMSE) of 0.27 °C and a bias of −0.17 °C. Statistics at R5, the other independent calibration section, are similar ($RMSE = 0.20$ °C, bias = −0.14 °C). Assessments of DTS error in previous laboratory and terrestrial field applications, also using single-ended systems, have shown smaller values for the RMSE, ≤ 0.15 °C, and bias, ≤0.05°C (Hausner et al., 2011; Suárez et al., 2011).

Several factors likely contributed to errors in this application, in addition to instrument error. First, the along-isobath orientation of the cable limits the range of observed temperatures. Second, the bath on the tower was not controlled at a constant temperature and fluctuated on a diurnal cycle. As a result, temperatures at different calibration sections were often too similar to constrain the parameters in equation (1). Finally, the sensors at R4, R5, and R6 were attached to the cable as it was rapidly being spooled off the stern of a ship. GPS positions were used to relate the time that each sensor was deployed to the distance along the cable, but there may be errors in the estimate of the distance d in (1).

After evaluating the measurements as described above, a final DTS data set was created for the analysis that follows in section 4. For this final data set, in order to estimate the calibration coefficients, the DTS backscatter data were fit to all five independent measurements along the cable using a least squares fit to (1). The final data set therefore makes use of all available calibration points. In this final data set, the measurement error at the western end of the cable can be evaluated by comparing the independent measurements of

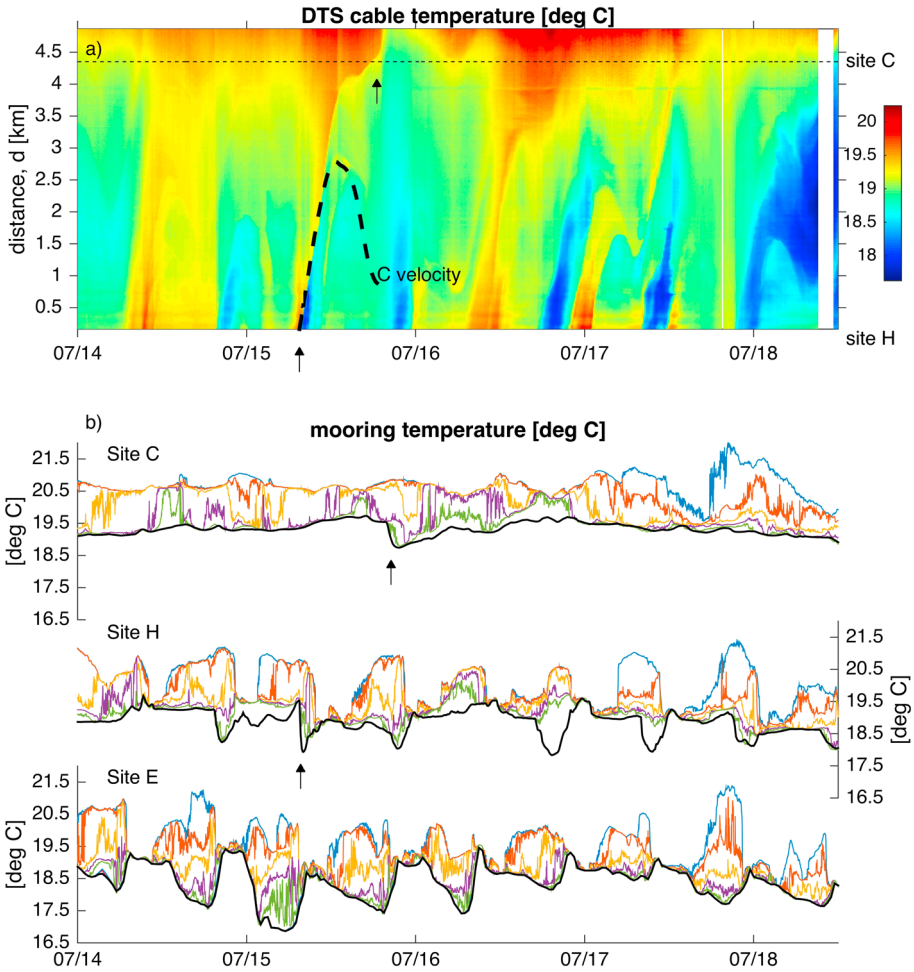

Figure 4. Along-shelf variations in temperature variability during 14–18 July. (a) Bottom temperature along DTS cable. Distance $d = 0$ is at site H. Locations of sites C and H are labeled. Dotted black line indicates the corner where the cable turns onshore near site C. Black dashed curve indicates hypothetical change in alongshore position calculated from near-bottom velocity at site C (velocity data from site H is not available during this time period). (b) Temperature throughout water column at three mooring sites C, H, and E. Black arrows indicate the arrival of a cold front at site H and later at site C. DTS = distributed temperature sensing.

bottom temperature at mooring site C and the nearest DTS measurement interval, which are separated by a distance of 435 m. This comparison results in an RMSE of 0.11 °C and a bias of 0.02 °C. The period after 5 September is characterized by weaker thermal stratification at the mooring sites, decreased alongshore variability along the DTS cable, and reduced availability of DTS data that pass the quality control procedures. During this period, the RMSE is reduced to 0.05 °C, likely due to more uniform temperatures between the two locations being compared. The analysis focuses primarily on the stratified time period from the start of the DTS record on 13 July through 5 September.

4. Subsurface Fronts Revealed by High-Resolution Observations

4.1. Alongshore Temperature Variability at Short Temporal and Spatial Scales

The detailed characteristics of short-term temporal variability, as well as small-scale spatial variability in the alongshore direction, are revealed by the DTS observations in combination with the moored array. A focused presentation of two subsets of observations spanning 4.5 days each, described next, offers clues about the potential drivers of small-scale variability between the mooring sites and along the DTS cable. In the first subset, from 14 July to 18 July (Figure 4), the water column near the western end of the DTS cable at site C is characterized by persistent thermal stratification (Figure 4b). A rapid drop in bottom temperature occurs on 15 July but otherwise, bottom temperature is relatively stable in time. Observations from the DTS

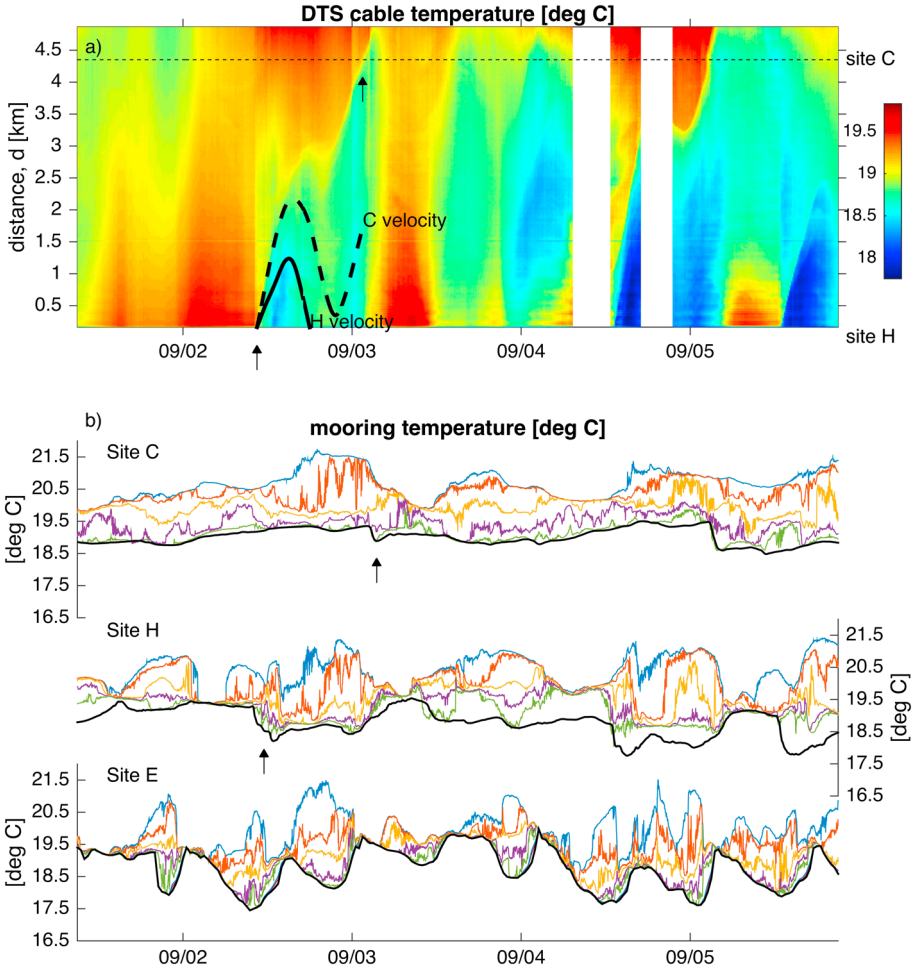

Figure 5. As in Figure 4 but for 1–5 September. The additional solid black curve indicates the hypothetical change in alongshore position calculated from near-bottom velocity at site H. DTS = distributed temperature sensing.

cable indicate that this near-bottom cooling at site C is linked to a strong cooling event that had occurred approximately 12 hr earlier at site H to the east (Figure 4, black arrows). A hypothetical alongshore position, estimated from the time integral of available velocity data 2 m above the seabed at site C, cannot fully explain the movement of the front down the cable during this time period (Figure 4, black curve). The initial westward movement of the front at site H is consistent with the alongshore velocity, but the arrival of the front at site C occurs during a phase of eastward flow. This suggests that the front is not only influenced by the alongshore currents but also advection of cooler water from offshore.

Observations from a different 4.5-day segment during 1–5 September, near the end of the stratified season, show similar patterns (Figure 5). During this period, relatively stable near-bottom temperatures at site C are interrupted by two near-bottom cooling events that travel down the cable over the course of a tidal cycle, for example, early on 3 September (Figure 5, black arrows). Once again, the alongshore velocity cannot fully explain the movement of the front down the cable. In this case, the timing of westward movement of the front is consistent with tidal modulation of alonghore flow, but the mean flow is not strong enough to explain the movement of the front all the way to site C. Velocity data from site H indicates a mean eastward flow, which does not help explain the discrepancy. As will be shown in section 4.4, these fronts have a three-dimensional structure that evolves as they progress westward and onshore.

In the moored observations, variability in the thermal structure of the water column changes dramatically with alongshore position. At the eastern sites, well-mixed waters appear roughly twice per day (Figures 4b and 5b). At site H, thermal stratification is interrupted by periods of uniform temperature from the surface to the bottom (Figure 4b). The oscillation between thermally well-mixed and stratified conditions is even

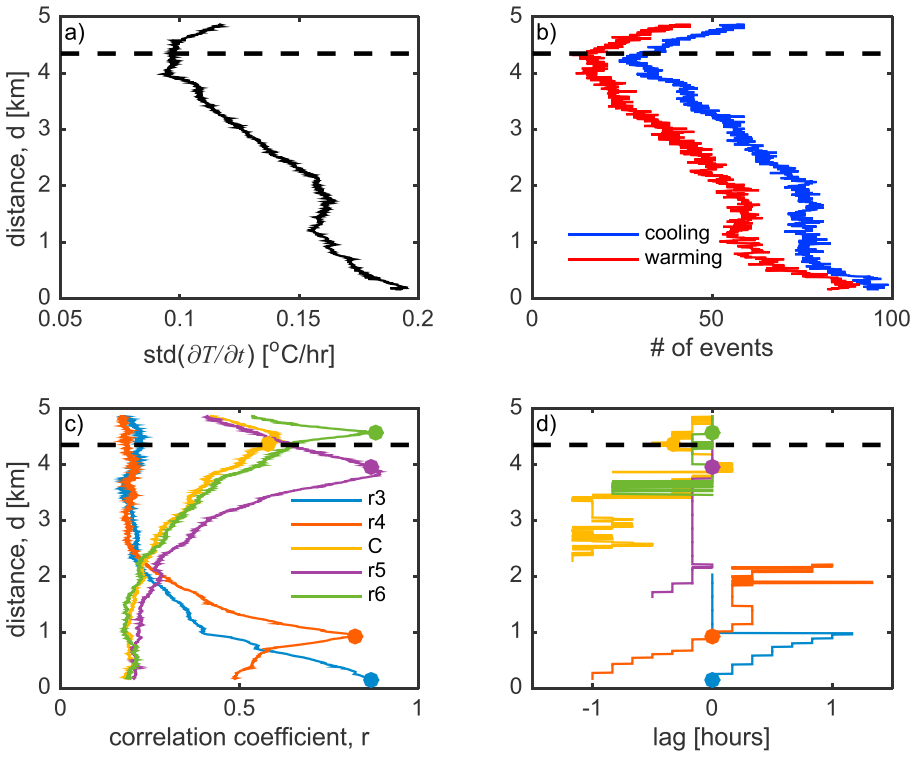

Figure 6. Descriptive statistics of temperature variability along the distributed temperature sensing (DTS) cable. (a) Standard deviation (std) of $\partial T/\partial t$. (b) Number of warming and cooling events exceeding the threshold $|\partial T/\partial t| > 0.25$ °C/hr. (c) Maximum lagged correlation between the time derivatives of bottom temperature ($\partial T/\partial t$) along the DTS cable and discrete bottom temperature sensors. Each solid line corresponds to a discrete sensor at a site in Figure 1. (d) Time lag of correlations in panel c. Positive values indicate that the point on the DTS cable lags the discrete sensor. In all panels, the dashed black line indicates the corner where the cable turns onshore near site C.

more apparent at site E (Figure 4b). There is a clear transition along the shelf, from more regular oscillations between stratified and unstratified conditions at site E to more persistent stratification at site C.

As shown above in section 2.3, thermal stratification at subtidal time scales is similar at sites C, H, and E when averaged over 2 days (Figure 2c). However, within the shorter time periods profiled here (Figures 4 and 5), the characteristics of high-frequency subsurface temperature variability change considerably over alongshore scales of 10 km and less. At sites H and E, the temporal variability of the thermal structure is consistent with signals associated with the semidiurnal tide. A lag in the onset of near-bottom cooling along the DTS cable, apparent during multiple events, indicates a component of propagation from east to west (Figures 4b and 5b). However, only a total of three cooling events propagate all the way to site C during these two time intervals, suggesting that the features either decay due to dissipative processes as they travel or have a limited along-shelf extent.

4.2. Spatial Structure of High-Frequency Bottom Temperature Variability

The time series presented above show examples of events that are characterized by relatively rapid near-bottom cooling, especially at the eastern end of the field site closer to Wasque Shoal. The DTS cable is now used to define, at high resolution, the spatial structure of temperature variance and the frequency of occurrence of warming and cooling events. Over the entire period analyzed, the standard deviation of $\partial T/\partial t$ is highest near site H and decreases from east to west toward site C (Figure 6a). This pattern is broadly consistent with the mooring time series at sites C and H (Figures 2a and 2b). The DTS cable also shows a segment of even variance (1 km $\leq d \leq$ 2 km) and a minimum in variance at the corner of the cable near site C (Figure 6a). At the end of the cable, variance increases toward shore.

To compare the frequency of occurrence of cooling and warming events at different locations, events are defined and quantified based on a threshold of $\partial T/\partial t$. Bottom temperature is filtered with a 30-min (three-point) running average, and a threshold of $|\partial T/\partial t| > 0.25$ °C/hr is used to classify events. The time of

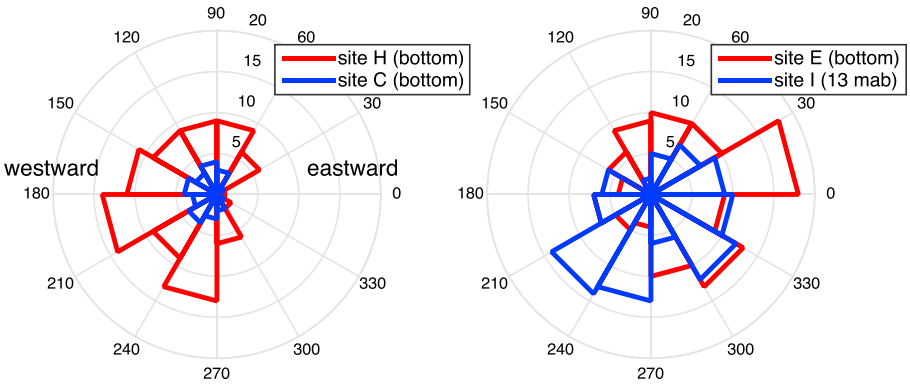

Figure 7. Polar histograms of rapid cooling events (as defined in the text), and their occurrence at different phases of the M_2 tidal cycle, at (a) sites C and H on opposite ends of the cable and (b) sites E and I, to the east and offshore of the cable, respectively. Radial distance indicates the number of events, with circular contours at 5, 10, 15, and 20 events. Angles indicate ranges of phase, with 0° representing peak tidal velocities to the east and 180° representing peak tidal velocities to the west.

an event is defined by the minimum or maximum in $\partial T/\partial t$. This threshold and averaging period are chosen so that changes in temperature are large enough and occur over a long enough time period that the events are not classified based on instrument noise. Counts of events occurring at each segment of the DTS cable show that cooling events are more frequent than warming events at all locations (Figure 6b). The greatest number of events occur at site H and the fewest occur at the corner of the cable near site C. At the end of the cable that is oriented in the cross-shelf direction, the number of events increases toward shore. The frequency of occurrence of the events along the cable has a similar spatial structure as the standard deviation of $\partial T/\partial t$ (Figures 6a and 6b). The similarity in horizontal structure of these metrics indicates that analysis of cooling events can be useful in investigating high-frequency temperature variability.

A cross-correlation analysis along the DTS cable is used to determine the decorrelation length scales of high-frequency temperature variability. Maximum lagged correlations are computed between time series of $\partial T/\partial t$ at each point along the DTS cable and all four in situ calibration points, as well as the bottom temperature at mooring site C (Figures 6c and 6d). At each calibration point (r3–r6), the highest correlation coefficients correspond to the nearest point on the DTS cable, which account for 68–78% of the variance. At site C, the maximum correlation with the cable is relatively low, accounting for only 34% of the variance, because the points are separated by a distance of 435 m. At all locations, the correlation with the DTS cable drops off rapidly with distance (Figure 6c). Decorrelation length scales, computed from the e-folding distances of the correlation coefficients with the calibration sites, range from 1,000–1,600 m. Time lags of the maximum correlation, computed at all locations above the noise floor at $r > 0.24$, show that locations on the eastern end of the cable tend to lead locations farther west (Figure 6d). This general pattern is consistent with a contribution of propagating features, such as those highlighted in section 4.1, to the overall variance at high frequencies. The short decorrelation length scales, and the reduction in variance along the cable, support the idea that these features are modified and dissipate as they travel from east to west.

4.3. Generation of Cooling Events Relative to the Tide

To connect the timing of cooling events with the tidal cycle, events are quantified at the three mooring sites that are distributed alongshore and in line with the cable axis near the 15-m isobath (sites C, H, and E) and one site located just offshore on the 22-m isobath (site I) for comparison. The timing of events is compared to the phase of the M_2 tidal cycle, as determined by a harmonic fit to the entire record of near-bottom velocity 2 m above the seabed at site H using T_Tide (Pawlowicz et al., 2002), which accounts for 78% of the variance. Histograms of the near-bottom cooling events occurring at the three sites near the 15-m isobath (sites H, C, and E) reveal that they occur most frequently at the eastern end of the study site closer to Wasque Shoal (Figure 7). Of these three sites, the most events occur at site E farthest to the east, and they occur most often when the M_2 tidal velocities are directed eastward (Figure 7b). Compared with 105 events observed at site E, 90 events are observed farther west at site H (Figure 7). At site H, the events occur mostly during the westward phase of the M_2 tide, consistent with a time lag in the arrival of cold water at these sites (Figure 7a). In contrast to these two sites on the eastern side of the study area, fewer events (28 total) are observed at site C

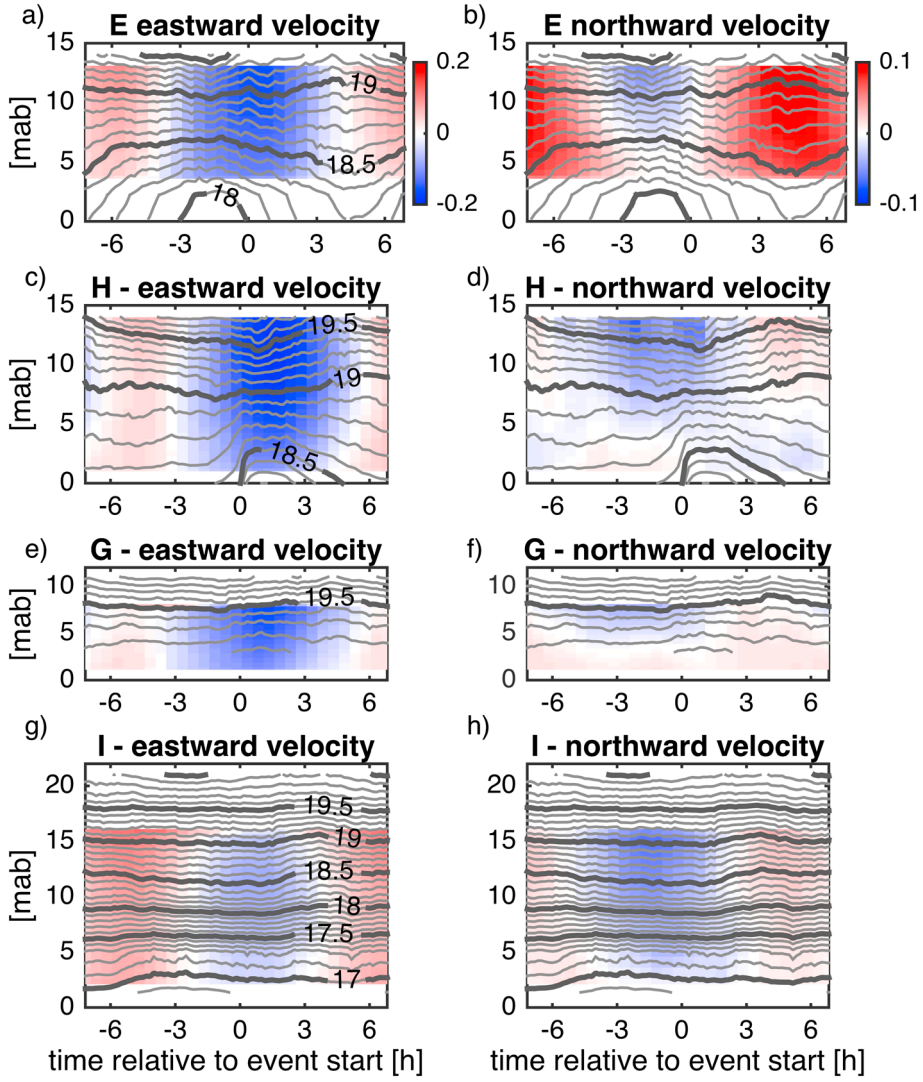

Figure 8. Composite averages of half-day periods centered around rapid cooling events at site H. Zero time corresponds to the time of minimum $\partial T/\partial t$ at H. (a) Composite average of water column temperature (contours) and eastward velocity (colors) at site E, during cooling events observed at site H. (b) Composite average of water column temperature (contours) and northward velocity (colors) at site E, during cooling events observed at site H. Contours are spaced at intervals of 0.1 °C. Velocity units are in meters per second. Note the difference in color scale between the eastward and northward components. (c, d) As in panels a and b but at site H. (e, f) As in panels a and b but at site G during cooling events at site H. (g, h) As in panels a and b but at site I during cooling events at site H.

on the western end of the cable. Farther offshore at site I, only 45 events are observed near the bottom, but 92 are observed in the middle of the water column 13 m above the bottom. Relative to the phase of the M_2 tide, most of these middepth events occur during the transition from westward to eastward flow (Figure 7b). Since tidal velocity ellipses rotate clockwise and are not strongly polarized on this part of the inner shelf (Kirincich et al., 2013), the timing of these middepth events is consistent with onshore flow in the M_2 tidal cycle.

These patterns show that cooling events are more frequent and have greater amplitude toward the eastern end of the study area on the 15-m isobath. The general pattern of most events occurring at the eastern sites E and H, and less occurring at C, is not sensitive to the threshold used to define events. If the threshold is increased by 50%, events occur with the same relative distribution between sites (74, 67, and 13 occurring at sites E, H, and C, respectively). The timing of the events relative to the M_2 tidal cycle, and the proximity of the eastern sites to the shoals on the eastern end of Martha's Vineyard, suggest that topographic effects

and advection of gradients by tidal currents are important drivers of high-frequency variability in subsurface temperature.

4.4. The Dynamics of Cooling Events

4.4.1. Vertical Structure at the Eastern End

As shown above, cooling events occur near the seafloor with greater magnitude and frequency of occurrence near Wasque Shoal, at the eastern end of the study area. Composite averages of temperature and velocity from the moored observations are examined here to determine the vertical structure associated with these events. All composite averages are referenced at time $t = 0$ to events that occur at site H, but the progression of signals is shown by examining the vertical structure at sites E, G, and I (Figure 8). A total of 90 events are used in the analysis. Within the composite averages, standard errors for estimates of the mean and velocity temperature anomalies, after removing the mean of each event, are all less than 0.01 °C and 0.01 m/s near the bottom.

At site E, to the east of the cable, near-bottom cooling leads the arrival of the events at site H (Figure 8b). This temporal lead is consistent with the differences in the phase of the tide at which events occur (section 4.3, Figure 7). The transition to weaker stratification after the passage of the cooling event is consistent with the examples shown in Figure 4, which show strong tidal fluctuations in stratification at this site. At site H, the composite average of velocity shows a bottom-intensified northward flow preceding the cooling event, which is also associated with an increase in stratification (Figures 8c and 8d). In shallower water at site G, strong cooling is less evident but composite averages of velocity do show a thin layer of northward flow near the bottom (Figures 8e and 8f). In contrast, farther offshore at site I, there is little evidence of bottom intensified northward flow in the composite velocity profiles (Figures 8e and 8f). There is a slight shoaling of isotherms at middepth during a phase of northward flow, consistent with the timing relative to the M_2 tide shown above in section 4.3.

Even though the cross-shelf velocity is directed onshore near the bottom as events arrive at site H, a coherent cooling signal progresses alongshore from east to west at the sites near the 15-m isobath. This westward progression is consistent with the westward propagation of cooling signals down the DTS cable (Figures 4, 5). The sequence of events leading up to the cooling events that arrive at site E, and subsequently travel down the cable along the 15-m isobath, indicate that the formation of cold fronts at this site is due the combined effect of tidal variability and stratification in the presence of the shoals at the eastern end of Martha's Vineyard.

4.4.2. Propagation at the Western End

Although events appear to propagate to the west, as shown above, many cooling events do not travel all the way to site C, ~4 km to the west. Here the effect of tidal variability is less pronounced, and there are relatively fewer cooling events (Figure 7). Shown below, three sample cooling events illustrate major differences in the structure and propagation direction of individual events observed at site C (Figure 9). The first cooling event in the record at site C, detected on 15 July 2014 (Figure 9) is one example of a front that travels with a westward component from site H to site C. As shown previously, this event originates at the eastern end of the study area, having passed by site H 11 hr earlier (Figure 4, black arrows). Temperature time series near the corner of the DTS cable show that the cooling event arrives first on the eastern leg of the cable and is followed by a more gradual and spatially uniform warming (Figures 9a and 9b). The east-west component of velocity during this time period is dominated by tidal currents (Figure 9c). The cooling event is associated with onshore velocity near the bottom and an elevation of isotherms (Figure 9d). Even though this cooling event is associated with onshore flow near the bottom, the arrival times at the corner of the cable (Figure 9a) and the 11-hr lag between arrival times at sites H and C (Figure 4) show that there is an alongshore component of propagation.

A different type of cooling event, during which there is no evidence of alongshore propagation, occurs on 26 July. The front arrives at all points on the main east-west oriented section of the cable between sites H and C at nearly the same time (Figures 9e and 9f), indicating the front is traveling perpendicular to the cable in the cross-shore direction. This event occurs on the eastward phase of the tide and is also associated with a bottom-intensified onshore flow in the cross-shore direction (Figures 9g and 9h). Unlike the first event, the cooling signal is stronger at site C than site H, showing that even onshore-propagating signals can be associated with alongshore temperature variability.

Finally, near the end of the stratified season, a cooling event on 3 September occurs at site C, which is different from the previous two examples in several ways. As shown previously, like the first event, the signal

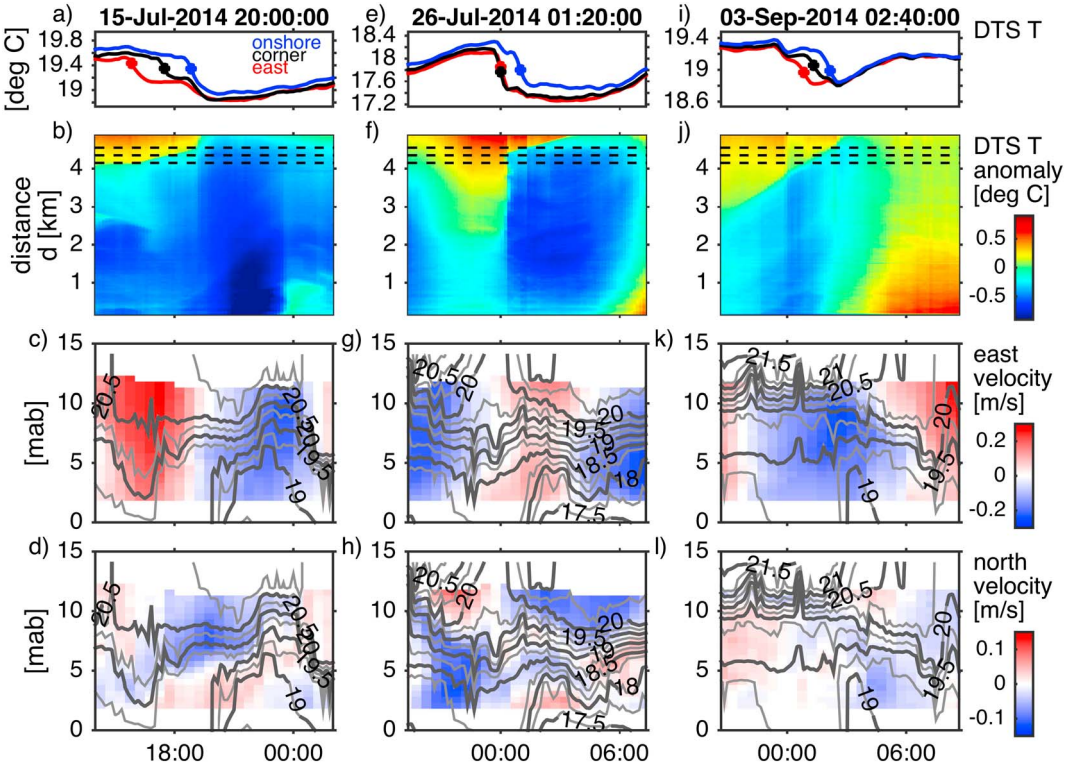

Figure 9. Time series of temperature and velocity during cooling events observed at site C on 15 July 2014 (a–d), 26 July 2014 (e–h), and 3 September 2014 (i–l). (a, e, i) Thirty-minute running averages of DTS temperature at three locations: the corner of the DTS cable closest to site C (black), 200 m along the cable in the onshore direction (blue), and 200 m toward the east (red). Circles indicate arrival times of the front based on minima in $\partial T/\partial t$. (b, f, j) DTS temperature anomalies along the entire cable length during the same time period, relative to the temperature during arrival at the corner of the cable (i.e., the black circle in the upper row). Dashed lines indicate positions of points shown in panel a. (c, g, k) Vertical structure of eastward velocity (colors) and temperature (contours) at site C. Contour interval is 0.25 °C. (d, h, l) As in panel c but with colors representing northward velocity. Note difference in velocity range. DTS = distributed temperature sensing.

progresses westward from site H to site C (Figures 5, 9i, and 9j). However, the event occurs during a period of strong westward flow and is not associated with a strong bottom intensified onshore flow as the previous two events (Figures 9k and 9l).

Viewed together, these three events show that there is not a consistent vertical or lateral structure of the cooling events that occur near site C. However, each are associated with relatively strong cooling that varies in arrival time along the cable, followed by a more gradual and more spatially uniform warming (Figures 9a, 9e, and 9i). Importantly, the varying magnitudes of alongshore versus cross-shore propagation suggest that the fronts seen at this location have multiple origins not all of which can be linked to tidal variability at the eastern end of the study area.

4.4.3. Phase Velocity Estimates

The corner of the cable at C provides a multiscale, two-dimensional array that can be used to compute robust estimates of the horizontal propagation characteristics of the fronts associated with near-bottom cooling. For each event, multiple estimates of phase velocity are calculated by triangulating front arrival times at different sets of three points near the corner of the DTS cable. For each estimate, a triangle is formed from the corner point on the DTS cable, one point farther onshore and another point farther to the east. Arrival times at the corner point (t_c), onshore point (t_o), and east point (t_e) are calculated based on the minimum value of $\partial T/\partial t$, as in section 4.4.1 (e.g., Figure 9, top row). The direction of propagation, ϕ, is calculated following Lee (1961),

$$\phi = \theta - \tan^{-1}\left[\frac{L_{oc}(t_e - t_c)}{L_{ec}(t_o - t_c)}\csc\xi - \cot\xi\right], \quad (2)$$

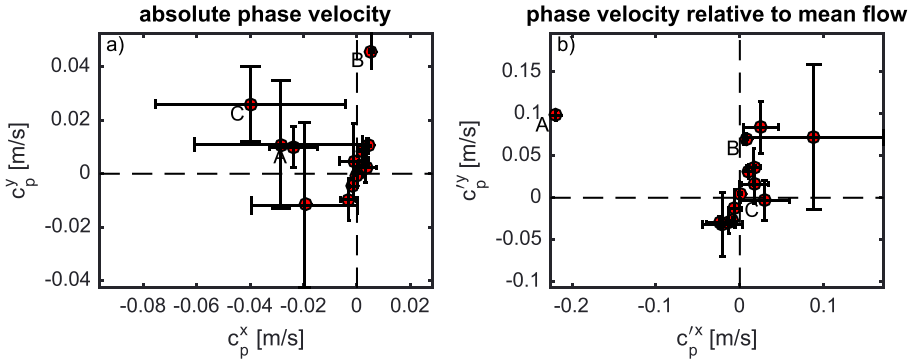

Figure 10. Phase velocity estimates for all cooling events detected at site C, using all estimates where $\Delta d \leq 75$ m. (a) Absolute phase velocity, without subtraction of depth-averaged currents. (b) Phase velocity relative to mean flow, with depth-averaged currents subtracted. Letter labels correspond to the events shown in Figure 9: 15 July (A), 26 July (B), and 3 September (C). In each panel, circles represent the mean and error bars represent the standard deviation. Note the difference in velocity scales between the two panels.

where L_{oc} is the distance between the corner and onshore points, L_{ec} is the distance between the corner and the east points, ξ is the angle made by the triangle legs L_{oc} and L_{ec}, and θ is the angle made by triangle leg L_{oc} and the x axis. The magnitude of the phase velocity vector c_p is then given by

$$|\boldsymbol{c}_p| = \frac{L_{oc}}{t_o - t_c} \cos(\theta - \phi). \tag{3}$$

To correct for the influence of background currents, the phase velocity relative to the depth-averaged flow is calculated as

$$\boldsymbol{c}'_p = \boldsymbol{c}_p - \bar{\boldsymbol{u}} \cdot \hat{\boldsymbol{\phi}}, \tag{4}$$

where $\bar{\boldsymbol{u}}$ is the depth-averaged velocity and $\hat{\boldsymbol{\phi}}$ is the unit vector in the direction of phase propagation. Only the component of $\bar{\boldsymbol{u}}$ in the direction of the front propagation is subtracted to estimate $\boldsymbol{c}'_p$. The depth-averaged velocity is averaged in time from the first to the last arrival times at the three cable sections used in the phase velocity calculations. Assuming that the front is straight and not curved, the background currents parallel to the front do not affect its propagation speed.

The DTS observations provide multiple estimates of the phase velocity, made over a range of scales that are averaged here to create a robust sampling of the frontal propagation. Estimates were made using triangles that contain the corner point and two additional points separated by from the corner by along-cable distances of up to 75 m. In order to avoid inclusion of the inconsistent estimates at small spatial scales, outliers of each calculated vector component are detected using a modified Z-score method based on deviations from the median (Iglewicz & Hoaglin, 1993). The standard deviation of the different estimates measured by the DTS cable is used to quantify the potential error in each phase velocity estimate.

Like the examples shown in the previous section, the resulting phase velocities show that the cooling events at site C have diverse characteristics and origins (Figure 10). When the currents are included in the phase velocity estimate, most events are aligned primarily in the onshore direction, including the event on 26 July highlighted in the previous section (Figure 10a). However, there are also several events that have a strong westward component, including the two events on 15 July and 3 September that have already been shown as examples of alongshore propagation. When the currents are removed from the phase velocity estimate, the first event (A) on 15 July is revealed as distinct from the other cooling events (Figure 10b). The initial arrival of this event occurs during an eastward phase of tidal flow (Figures 9a–9d), which indicates that it is propagating against the current. In contrast, the later event on 3 September (C) occurs on the westward phase of the tide (Figure 9k), and its phase velocity decreases to nearly 0 when the tidal currents are removed (Figure 10b). Alongshore advection of the front by the background flow can greatly influence the absolute propagation speed of the front observed at site C. However, the role of alongshore advection by tidal currents is less consistent than at site H, affecting some events but not others. In addition, many of the phase velocities are aligned in the onshore direction, indicating that onshore propagation and advection by tidal currents are both important drivers of variability at this site.

4.4.4. Comparison With Theoretical Propagation Speeds

To identify potential processes other than advection that influence cooling events observed at site C, observed propagation speeds are compared with theoretical speeds of gravity currents and internal waves. These theoretical predictions are highly simplified, but they can be used as scaling parameters in model experiments or more detailed theoretical studies (e.g., Venayagamoorthy & Fringer, 2007; White & Helfrich, 2008). Comparing them with observations may therefore guide future work on alongshore variability associated with propagating fronts over the inner shelf. In an idealized gravity current, a layer of dense water intrudes into lighter ambient water at a front that intersects the seabed. The propagation speed of a gravity current in the absence of friction (Benjamin, 1968) is given by

$$c_{gc} = \sqrt{gh(\rho_1 - \rho_2)/\rho_2} = \sqrt{g'h}, \tag{5}$$

where g is gravitational acceleration, h is total water depth, ρ_1 is the density of the heavier fluid within the gravity current, ρ_2 is the density of the lighter ambient fluid, and g' is the reduced gravity. In the presence of friction, the gravity current speed is expected to be reduced. The propagation speed of linear, hydrostatic internal waves in shallow water, with linearly varying stratification, is given by

$$c_w = \frac{Nh}{n\pi}, \tag{6}$$

where $N = \sqrt{-\frac{g}{\rho_o}\frac{\partial \rho}{\partial z}}$ is the buoyancy frequency and n is an integer corresponding to the wave mode (Kundu & Cohen, 2004). The theoretical phase speeds given by (5) and (6) are highly simplified and do not account for bathymetric variations, vertically sheared background currents, vertical variations in stratification, or three-dimensional circulation patterns. However, they can be estimated from available observations, and each is estimated from a different aspect of the density field. The gravity current speed (5) is related to horizontal density gradients across a front along the bottom, while the internal wave speed (6) is related to the background vertical density gradient.

The theoretical gravity current phase speed, c_{gc}, is computed for each event using the bottom temperature at site C. Density is estimated from temperature using a linear regression from shallower sensors at site C where salinity observations are available ($R^2 = 0.92$). The horizontal density difference is estimated from temperature values 1 hr before and after the arrival the front at site C. A significant correlation, at the 95% confidence level, is found in comparing the theoretical gravity current phase speed estimates, c_{gc}, with the observed cross-shore component of the phase velocity, c_p^y (Figure 11a). However, the regression line shows that the observed onshore components of phase velocity are overestimated by the theoretical gravity current speeds. After adjustment of the phase speeds for the background currents, the cross-shore component $c_p'^y$ is significantly, but more weakly, correlated with the theoretical gravity current speeds (Figure 11b). Although the regression slope is closer to 1, the theoretical prediction still overestimates the observations. The correlation with total magnitude of the observed phase speed $|c_p|$ is only significant before adjustment for the background currents ($r = 0.67, p < 0.01$, not shown). The significance of the correlations do not depend on the particular time lags used. The correlations shown remain significant if the temperatures 30 min before and after the event arrival are used to estimate the horizontal density difference and improve slightly if the temperature at the time of the arrival is used for computing ρ_2.

Estimates of the theoretical shallow-water internal wave speed are less successful in explaining the observed phase speeds. Different estimates of the vertical density gradient were estimated using the bottom temperature at C and all other sensors on the mooring. These five different estimates of stratification were computed at both the time of arrival and 1 hr before. Correlation of these estimates of c_w and observed estimates of the phase speeds ($|c_p|$, $|c_p'|$), as well as the observed alongshore components of phase velocity (c_p^y, $c_p'^y$), were all found to be insignificant at the 95% confidence level except for two comparisons with negative regression coefficients (not shown).

In summary, comparisons with theoretical predictions show a weak but statistically significant relationship between the observed cross-shore component of phase velocity and the theoretical gravity current speed. The differences in magnitude between observations and theory could be due to the influence of friction and a sloping bottom. It appears that advection by background currents is more influential in the alongshore component, in which the tidal currents and mean flow tend to be stronger. The presence of strong tidal currents can lead to significant errors in the calculation of phase velocity relative to the mean flow, as shown

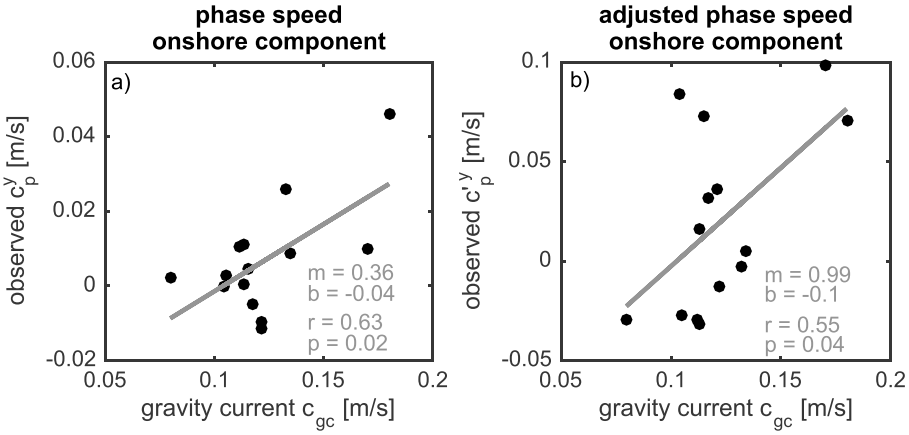

Figure 11. Comparison of observed frontal phase velocity estimates with gravity current speeds estimated from classical theory (5). (a) Regression of estimated gravity current speed c_{gc} to observed onshore phase speed, c_p^y, before adjusting for background currents. (b) Regression of estimated gravity current speed c_{gc} to observed onshore phase speed, $c_p'^y$, after adjusting for background currents.

in Figure 10. These errors, in addition to those associated with complex curvature of the fronts, may account for offshore-directed phase velocities. Although the results suggest that the observed cooling events are not strongly influenced by linear internal wave dynamics, the role of internal waves propagating from offshore cannot be ruled out. In particular, nonlinear internal bores generated farther offshore may be contributing to high-frequency variability at this site.

5. Discussion

5.1. Synthesis of Observations

By combining DTS technology with moored observations, this unique set of observations captures an unprecedented view of small-scale lateral variability over the inner continental shelf, revealing significant alongshore variability at high-frequency, superinertial time scales. Alongshore variability is present in both the small-scale spatial structure of individual events and in the temporal statistics of the near-bottom temperature. Time series of $\partial T/\partial t$ are characterized by short decorrelation scales of 1,000–1,600 m (section 4.2). Along the 15-m isobath, the eastern end of the study site is characterized by stronger high-frequency variability in terms of the number and magnitude of rapid cooling events, as well as high-frequency variance in near bottom temperature (sections 2.3 and 4.2). This site is closer to shoaling bathymetry that interrupts the relatively straight isobaths.

The circulation patterns associated with cooling events highlighted here are complex and three dimensional. Tidal currents in the alongshore direction play a major role in advecting gradients associated with subsurface fronts. At locations close to Wasque Shoal in the east, the timing of rapid cooling events is strongly linked with the phase of M_2 tidal velocities. The arrival times of cold bottom water, warm mixed water, and horizontal temperature fronts are depicted schematically in Figure 12. To the east of the cable deployment, at site E, most near-bottom cooling events occur when the tidal velocities are directed eastward (Figure 7b). The vertical structure of temperature at this site changes dramatically with tidal cycle, alternating between weak and strong stratification (Figures 4b and 5b). Slightly farther to the west at site H (the start of the cable) the most rapid cooling occurs during westward tidal flow (Figures 7b and 8a). Here minimum temperatures are also associated with increased stratification (Figures 4b, 8a, and 8b). At longer time scales, periods of strong stratification are associated with elevated high-frequency temperature variability (section 2.3).

In addition to being influenced by alongshore tidal velocities, cooling events observed at the 15-m isobath are also associated with weaker cross-shelf circulation. Near-bottom cooling events at site H are preceded by bottom-intensified onshore flow, indicating that advection of cold water from offshore also plays a role in the near-bottom cooling. The DTS observations show that fronts travel westward down the cable, but many of them do not reach the western end at site C (Figure 4). Among the relative few events observed at site C, the onshore component of phase propagation is weakly correlated with the theoretical gravity current

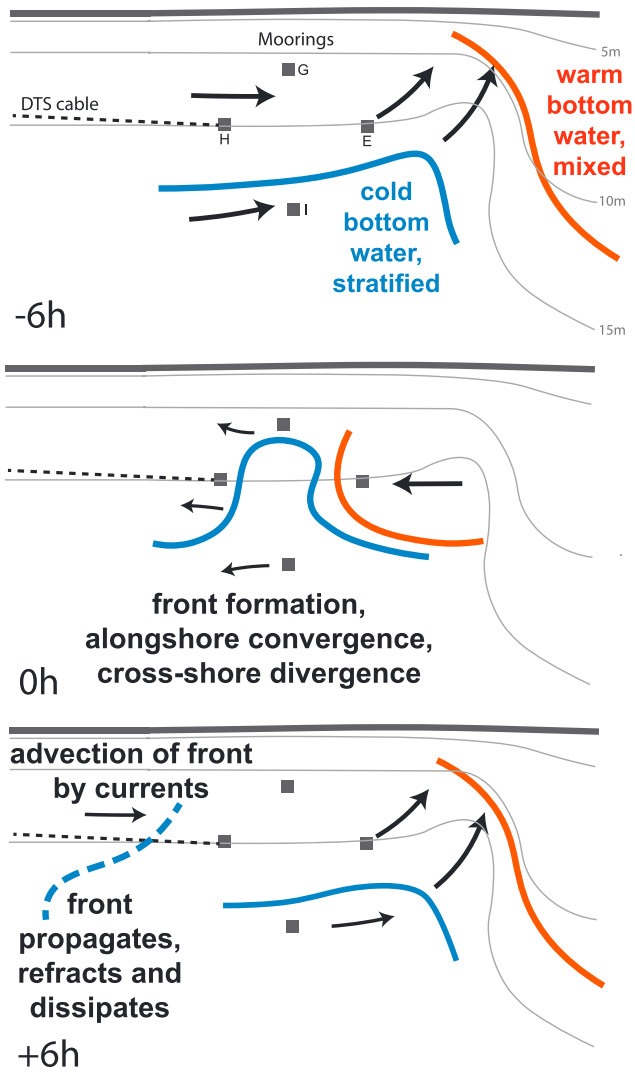

Figure 12. Plan view schematic summarizing observed variability associated with fronts at the eastern end of the study area. Currents and bottom temperature are shown at different phases of the tidal cycle, centered around a cooling event at site H at $t = 0$ hr, as in the composite averages in section 4.4.1. Arrows indicate currents, gray squares indicate mooring locations, the black dashed line shows the eastern portion of the DTS cable, and solid gray lines indicate topography. Over the shallow bathymetry of Wasque Shoal, strong vertical mixing by tidal currents is associated with warm bottom water (orange). A dynamic tidal mixing front separates this well-mixed water from colder bottom water at stratified locations (blue). Note that the dynamics of the western end of the study area, including mooring site C, are less directly influenced by the tidal mixing front and not shown here. DTS = distributed temperature sensing.

phase speed (5) at that location. Propagating fronts observed at site C likely originate from multiple sources, including remote locations farther offshore.

5.2. Processes Driving Propagating Fronts

Different processes govern the timing and magnitude of cooling events at different locations along the shelf, as high-frequency variance and the number of observed events decrease from east to west. Near Wasque Shoal, near-bottom cooling events are strongly influenced by the M_2 tide. Here the cooccurrence of near-bottom cooling with strong stratification and eastward velocity at tidal time scales is consistent with advection of a tidal mixing front. Based on criteria of h/U^3 (Simpson & Hunter, 1974), where h is water depth and U is tidal velocity, the combination of shallow shoals and strong tidal currents on the eastern part of the Martha's Vineyard inner shelf are expected to result in a sharp boundary between stratified and unstratified water (Wilkin, 2006). At the easternmost site E, the regular oscillation between highly stratified and mixed conditions indicates that its location is close to the mean position of the tidal mixing front (Figure 12) and subject to direct influence by tidal advection.

Slightly farther west at H, the eastern end of the cable, the influence of the tidal mixing front is less direct. Typical tidal velocities of ~0.3 m/s at the eastern end of the study area (Kirincich et al., 2013; Kirincich, 2016) correspond to a tidal excursion of ~4.6 km, which exceeds the 3.5-km distance between these two sites. However, oscillations in near-bottom temperatures at site H are less regular than those farther east (Figure 4), and there are fewer near-bottom cooling events (section 2.3). Near-bottom cooling events at site H mostly occur during the westward phase of the M_2 tide, just before the arrival of the unstratified water from the east (Figures 4, 7, and 8).

The differences in timing in the arrival of cold water, at different phases of the M_2 tide, indicate that it originates from a localized pool of cold water adjacent and offshore of the two sites H and E. Tidal currents increase in magnitude from west to east across the study area, and the tidal ellipses become more circular moving away from the coast at the eastern end (Kirincich et al., 2013). The circular tidal ellipses, in combination with a cyclonic mean flow, allow for cold water to be advected from offshore, toward the 15-m isobath. Localized advection can then set up sharp horizontal gradients near site H, where passing fronts are characterized by rapid changes in temperature (Figures 4 and 8) and are preceded by a bottom-intensified onshore flow (Figure 8).

The close relationship between the near-bottom cooling events and M_2 tidal velocities at the eastern end of the study site, close to Wasque Shoal, suggests that the subsurface fronts at this location are predominantly generated locally on the inner shelf rather than remotely generated at the shelf break or beyond. The shelf break is a potential generation site for internal waves, solitons, and bores (MacKinnon & Gregg, 2003a; Shearman & Lentz, 2004). However, baroclinic tidal motions and nonlinear internal waves experience significant dissipation while traveling across the wide continental shelf of southern New England (Shearman & Lentz, 2004). Internal waves of elevation may form bores in shallow water from nonlinear internal waves generated offshore of the shelf break (Shroyer et al., 2009), but these nonlinear waves are generally not predictable (Nash et al., 2012). In contrast, internal bores in the nearshore can be phase locked with the barotropic tide near locations of strong bathymetric variability, such as the head of a submarine canyon (e.g., Walter & Phelan, 2016). It is therefore likely that the near-bottom cooling events observed at the eastern end of the study area are generated locally on the inner shelf through interactions between tidal currents, local

complex bathymetry, and strong vertical and horizontal density gradients. However, farther to the west at site C, the tidal mixing front has less of a direct effect and onshore propagation is observed. It is therefore likely that internal bores generated remotely at offshore locations have a greater effect on the western end of the study area. The diverse characteristics of cooling events observed at the different sites, separated by less than 5 km, highlights the importance of considering small-scale alongshore variability over the inner shelf.

The observations along the DTS cable show that subsurface fronts set up by the three-dimensional tidal circulation can propagate to the west and onshore as a gravity current or cold-water tidal bore. Many of the fronts have limited alongshore extent in the DTS observations, either due to dissipation or finite width. A small fraction of near-bottom cooling events make it all the way to the western end of the cable at site C, progressing westward through a full phase of the tidal cycle. The phase velocities of propagating fronts at this site are weakly correlated with gravity current phase speeds in the onshore direction and are modulated by the background depth-averaged currents in the alongshore direction. As noted above, it is possible that the cooling events at this site might actually originate from a variety of sources. Internal bores generated at the shelf break have dynamics similar to gravity currents (Venayagamoorthy & Fringer, 2007) and would be consistent with the onshore phase velocity of many of the observed cooling events. However, the DTS observations also reveal fronts that propagate with an alongshore component and are clearly connected to variability farther east at site H, indicating that local generation of propagating fronts can also occur near shallow bathymetric features over the inner shelf.

The actual dynamics of the observed fronts are likely more complex than idealized gravity currents or internal waves due to the presence of friction, background currents, variable bathymetry, and ambient stratification. Similar to this study, high-frequency near-bottom temperature fluctuations, associated with velocities that are correlated with theoretical gravity current speed (5) and a regression slope indicating reduction by friction, have been observed in the kelp forest environment (Rosman et al., 2007). However, classical gravity current theory (5) is highly simplified; gravity current dynamics can be significantly altered by the presence of ambient stratification (Maxworthy et al., 2002; White & Helfrich, 2008). The relationships shown in Figure 11 suggest that, while advection by the background current influences the alongshore component of propagation in many cases, gravity current dynamics and the horizontal density gradient play a role in determining the cross-shore propagation of the fronts. Future studies should consider the potential role of alongshore variability in the generation and propagation of fronts driving high-frequency variability over the inner shelf.

5.3. Implications for Inner-Shelf Dynamics

Although few observational studies have addressed alongshore variations in high-frequency variability over scales of several kilometers and less, high-resolution sampling in the alongshore direction can reveal previously unobserved processes. Thorpe and Lemmin (1999) found strong alongshore variability at scales down to 50 m in the "internal wave surf zone" of a lake. Thomas et al. (2016) found alongshore variations in bottom pressure variance associated with rotation and spreading of nonlinear internal wave fronts. Alongshore variations can arise due to multiple factors, including the tidal excursion, finite extent of temperature fronts, and refraction associated with variations in phase speed due to changes in depth and background stratification. Therefore, tracer flux and exchange estimates at one location may not be representative of nearby sites.

High-resolution sensing of temperature at multiple scales using DTS, in combination with moored sensors, provides a means of observing small-scale baroclinic processes over long horizontal distances, complementing more commonly used moored, shipboard, and remote sensing techniques. Measuring only at the smallest ($\leq$100 m) or the largest ($\geq$4 km) scales of the observational array would have aliased the rapid cooling events and would yield different results and estimates of the along-shelf propagation. In addition, the subsurface structure of the cooling events means that they cannot be fully captured by remote sensing of the surface; high-resolution measurements of bottom temperature provide a valuable perspective on fine-scale subsurface features. The fronts are stronger and occur more frequently near shoaling bathymetry but can also influence other locations due to propagation and advection by background currents.

6. Summary

The combination of the DTS cable and and an array of moorings on the 15-m isobath of the Martha's Vineyard inner shelf provides an opportunity to examine both alongshore variability in temperature and the vertical structure of temperature and velocity. The characteristics of high-frequency temperature variance change dramatically over alongshore scales of several kilometers and temporal scales of days to weeks. Statistics from the DTS cable reveal the fine-scale horizontal structure of high-frequency bottom temperature variability. At the eastern end of the study area, close to the complex bathymetry of Wasque Shoal, the occurrence of near-bottom cooling events associated with fronts is linked to the phase of M_2 tidal currents and modulated by background stratification, consistent with local generation of a tidal mixing front. Only a few kilometers away, along the same isobath, subsurface fronts appear less frequently, and it is possible that many are remotely generated at offshore locations. A small fraction of the fronts travel all the way down the ~4-km alongshore extent of the DTS cable, but many weaken and dissipate. Among the fronts that do appear at the western end of the cable, the onshore component of phase velocity is broadly consistent with gravity current dynamics, while the alongshore component of phase velocity is strongly influenced by tidal currents. In addition to the influence of internal bores generated at offshore locations, the results of this study show that subsurface fronts generated in shallow water by the interaction of tidal currents, bathymetry, and stratification can be associated with alongshore variability over short scales of kilometers or less. It is possible that this mechanism for local generation and subsequent propagation of subsurface fronts occurs in other inner-shelf regions with nonuniform bathymetry and that high-resolution observations are needed to resolve the associated small-scale alongshore variability.

Appendix A: DTS Theory and Background

The measurement of temperature along the fiber-optic cable is based on the characteristics of backscattered light. Only a brief description of the measurement technique is given here; see reviews by Selker et al. (2006) and Tyler et al. (2009) for a more complete introduction and description of various applications in the environmental sciences. In short, a small portion of a pulse of light from a laser with a single frequency, ω, sent down a fiber-optic cable is scattered back up the cable as the light interacts with the fiber material. Most of the scattered light is due to Rayleigh scattering, which has the same frequency as the incident light of the laser and does not provide any indication of the temperature along the cable. A smaller portion of the scattered light is due to Raman scattering, which occurs when there is a transfer of energy between the light and molecules of the cable material. A loss of energy from a photon to the cable material results in a lower frequency in the scattered light, which is referred to as Stokes Raman scattering. Transfer of energy from the cable material to a photon results in a higher frequency in the scattered light, which is referred to as anti-Stokes Raman scattering. The ratio of the amount of Stokes scattering to anti-Stokes scattering is a function of temperature. A greater relative proportion of anti-Stokes scattering occurs at higher temperatures.

Commercially available DTS instruments contain a laser that emits light into the fiber-optic cable, as well as detectors that measure the intensity of Stokes and anti-Stokes backscatter. For a "single-ended" system, in which the DTS instrument is connected at one end of the cable only, the temperature may be calculated from the intensity of the backscatter according to (1) (Hausner et al., 2011). The parameter $\Delta\alpha$ accounts for the differences in the attenuation length scales between the Stokes and anti-Stokes backscatter. According to Beer's law, the attenuation length scale is a function of frequency, as well as the properties of the cable material. The calibration equation (1) assumes that $\Delta\alpha$ does not vary with distance along the cable (Hausner et al., 2011). Step losses over short distances can be corrected for, but damage over large portions of the cable due to strain are difficult to detect without overlapping measurements. The dimensionless parameter C accounts for the relative efficiency of the detectors that measure Stokes and anti-Stokes backscatter, which can vary with operating conditions such as instrument temperature and power supply. The parameter γ is proportional to the energy difference between the incident light and Raman scattered light, which is dependent on the frequency of the incident laser and cable material. In theory, $\gamma = \hbar\Delta\omega/k_B$, where $\hbar$ is Planck's constant, $\Delta\omega$ is the frequency shift of the backscatter, and k_B is Boltzmann's constant. In practice, however, γ also varies with operating conditions and is therefore treated as a calibration parameter (Hausner et al., 2011; van de Giesen et al., 2012). By calibrating the cable measurements with three separate temperature sensors, it is possible to compute the three calibration coefficients at each time and estimate temperature at all sections of the cable.

Acknowledgments
Deployment of the DTS system was made possible by the Center for Transformative Environmental Monitoring Programs (CTEMPS), with input, assistance, and software provided by John Selker, Scott Tyler, Paul Wetzel, Mark Hausner, and Scott Kobs. The authors thank Hugh Popenoe, Jared Schwartz, and Brian Guest for their technical expertise and effort with setup, deployment, and recovery of the DTS system, as well as the captains and crew of the R/V Discovery and R/V Tioga. Janet Fredericks assisted with integrating the DTS measurements with Martha's Vineyard Coastal Observatory infrastructure. Steve Lentz was instrumental in the design and deployment of the ISLE mooring array. Craig Marquette provided invaluable expertise and effort in the deployment of the ISLE mooring array. The authors thank Greg Gerbi for providing velocity data at site H and Malcolm Scully for providing velocity and near-bottom temperature data at site E. Kenneth Brink and two anonymous reviewers provided valuable comments on the manuscript. DTS measurements were supported by the Woods Hole Oceanographic Institution. The ISLE project is supported by NSF (OCE-83264600). T. Connolly acknowledges support from NSF (OCE-1433716) and a WHOI postdoctoral scholarship funded by the U.S. Geological Survey and the WHOI Coastal Ocean Institute. DTS data are available on Zenodo (Connolly & Kirincich, 2018, https://doi.org/10.5281/zenodo.1136113). ISLE mooring data are available on the WHOI Open Access Data Server (Kirincich & Lentz, 2017b, https://doi.org/10.1575/1912/8740).

References

Benjamin, T. B. (1968). Gravity currents and related phenomena. *Journal of Fluid Mechanics*, *31*(2), 209–248. https://doi.org/10.1017/S0022112068000133

Bogucki, D., Dickey, T., & Redekopp, L. G. (1997). Sediment resuspension and mixing by resonantly generated internal solitary waves. *Journal of Physical Oceanography*, *27*, 1181–1196. https://doi.org/10.1175/1520-0485(1997)027<1181:SRAMBR>2.0.CO;2

Castelao, R., Chant, R., Glenn, S., & Schofield, O. (2009). The effects of tides and oscillatory winds on the subtidal inner-shelf cross-shelf circulation. *Journal of Physical Oceanography*, *40*(4), 775–788. https://doi.org/10.1175/2009JPO4273.1

Chen, C., & Beardsley, R. C. (1995). A numerical study of stratified tidal rectification over finite-amplitude banks. Part I: Symmetric banks. *Journal of Physical Oceanography*, *25*(9), 2090–2110. https://doi.org/10.1175/1520-0485(1995)025<2090:ANSOST>2.0.CO;2

Colosi, J. A., Beardsley, R. C., Lynch, J. F., Gawarkiewicz, G., Chiu, C.-S., & Scotti, A. (2001). Observations of nonlinear internal waves on the outer New England continental shelf during the summer Shelfbreak Primer study. *Journal of Geophysical Research*, *106*(C5), 9587–9601. https://doi.org/10.1029/2000JC900124

Connolly, T. P., & Kirincich, A. R. (2018). Distributed temperature sensing and associated data—Martha's Vineyard Coastal Observatory 2014, Zenodo. https://doi.org/10.5281/zenodo.1136113

Emery, W. J., & Thomson, R. E. (2004). *Data Analysis Methods in Physical Oceanography* (2nd ed.). The Netherlands: Elsevier Science B V. Amsterdam.

Farrar, J. T., Zappa, C. J., Weller, R. A., & Jessup, A. T. (2007). Sea surface temperature signatures of oceanic internal waves in low winds. *Journal of Geophysical Research*, *112*, c06014. https://doi.org/10.1029/2006JC003947

Fewings, M. R., & Lentz, S. J. (2011). Summertime cooling of the shallow continental shelf. *Journal of Geophysical Research*, *116*, C07015. https://doi.org/10.1029/2010JC006744

Ganju, N. K., Lentz, S. J., Kirincich, A. R., & Farrar, J. T. (2011). Complex mean circulation over the inner shelf south of Martha's Vineyard revealed by observations and a high-resolution model. *Journal of Geophysical Research*, *116*, C10036. https://doi.org/10.1029/2011JC007035

Hausner, M. B., Suárez, F., Glander, K. E., van de Giesen, N., Selker, J. S., & Tyler, S. W. (2011). Calibrating single-ended fiber-optic Raman spectra distributed temperature sensing data. *Sensors*, *11*, 10,859–10,879. https://doi.org/10.3390/s111110859

Horwitz, R., & Lentz, S. J. (2014). Inner-shelf response to cross-shelf wind stress: The importance of the cross-shelf density gradient in an idealized numerical model and field observations. *Journal of Physical Oceanography*, *44*, 86–103. https://doi.org/10.1175/JPO-D-13-075.1

Iglewicz, B., & Hoaglin, D. (1993). How to detect and handle outliers. In E. F. Mykytka (Ed.), *ASQC basic references in quality control: Statistical techniques* (Vol. 16). Milwaukee, WI: Quality Press, A S Q C.

Kim, S. Y. (2010). Observations of submesoscale eddies using high-frequency radar-derived kinematic and dynamic quantities. *Continental Shelf Research*, *30*(15), 1639–1655. https://doi.org/10.1016/j.csr.2010.06.011

Kirincich, A. (2016). The occurence, drivers, and implications of submesoscale eddies on the Martha's Vineyard inner shelf. *Journal of Physical Oceanography*, *46*, 2645–2662. https://doi.org/10.1175/JPO-D-15-0191.1

Kirincich, A. R., & Barth, J. A. (2009). Alongshelf variability of inner-shelf circulation along the central Oregon coast during summer. *Journal of Physical Oceanography*, *39*(6), 1380–1398. https://doi.org/10.1175/2008JPO3760.1

Kirincich, A. R., & Lentz, S. J. (2017a). The importance of lateral variability on exchange across the inner shelf south of Martha's Vineyard, MA. *Journal of Geophysical Research: Oceans*, *122*, 2360–2381. https://doi.org/10.1002/2016JC012491

Kirincich, A. R., & Lentz, S. J. (2017b). *Inner shelf lateral exchange*. Woods Hole, MA: Woods Hole Open Access Server (WHOAS). https://doi.org/10.1575/ 1912/8740

Kirincich, A. R., Lentz, S. J., Farrar, J. T., & Ganju, N. K. (2013). The spatial structure of tidal and mean circulation over the inner shelf south of Martha's Vineyard, Massachusetts. *Journal of Physical Oceanography*, *43*, 1940–1958. https://doi.org/10.1175/JPO-D-13-020.1

Kundu, P. K., & Cohen, I. M. (2004). *Fluid Mechanics* (3rd ed.). Amsterdam: Elsevier.

Leary, P. R., Woodson, C. B., Squibb, M. E., Denny, M. W., Monismith, S. G., & Micheli, F. (2017). Internal tide pools prolong kelp forest hypoxic events. *Limnology and Oceanography*, *62*(6), 2864–2878. https://doi.org/10.1002/lno.10716

Lee, O. S. (1961). Observations on internal waves in shallow water. *Limnology and Oceanography*, *6*, 312–321.

Lentz, S. J. (2008). Seasonal variations in the circulation over the Middle Atlantic Bight continental shelf. *Journal of Physical Oceanography*, *38*, 1486–1500.

Lentz, S. J., Churchill, J. H., Marquette, C., & Smith, J. (2013). Evaluation and recommendations for improving the accuracy of an inexpensive water temperature logger. *Journal of Atmospheric and Oceanic Technology*, *30*, 1576–1582. https://doi.org/10.1175/JTECH-D-12-00204.1

Lentz, S. J., & Fewings, M. R. (2012). The wind- and wave-driven inner-shelf circulation. *Annual Review of Marine Science*, *4*, 317–343. https://doi.org/10.1146/annurev-marine-120709-142745

Loder, J. W., Drinkwater, K. F., Oakey, N. S., & Horne, E. P. W. (1993). Circulation, hydrographic structure and mixing at tidal fronts: The view from Georges Bank. *Philosophical Transactions of the Royal Society London A*, *343*(1669), 447–460. https://doi.org/10.1098/rsta.1993.0058

MacKinnon, J. A., & Gregg, M. C. (2003a). Mixing on the late-summer New England shelf: Solibores, shear, and stratification. *Journal of Physical Oceanography*, *33*(7), 1476–1492. https://doi.org/10.1175/1520-0485(2003)033<1476:MOTLNE>2.0.CO;2

MacKinnon, J. A., & Gregg, M. C. (2003b). Shear and baroclinic energy flux on the summer New England shelf. *Journal of Physical Oceanography*, *33*(7), 1462–1475. https://doi.org/10.1175/1520-0485(2003)033<1462:SABEFO>2.0.CO;2

Maxworthy, T., Leilich, J., Simpson, J. E. J. H., & Meiburg, E. H. (2002). The propagation of a gravity current into a linearly stratified fluid. *Journal of Fluid Mechanics*, *453*, 371–394. https://doi.org/10.1017/S0022112001007054

Nam, S., & Send, U. (2011). Direct evidence of deep water intrusions onto the continental shelf via surging internal tides. *Journal of Geophysical Research*, *116*, C05004. https://doi.org/10.1029/2010JC006692

Nash, J. D., Kelly, S. M., Shroyer, E. L., Moum, J. N., & Duda, T. F. (2012). The unpredictable nature of internal tides on continental shelves. *Journal of Physical Oceanography*, *42*(11), 1981–2000. https://doi.org/10.1175/JPO-D-12-028.1

Nidzieko, N. J., & Largier, J. L. (2013). Inner shelf intrusions of offshore water in an upwelling system affect coastal connectivity. *Geophysical Research Letters*, *40*, 5423–5428. https://doi.org/10.1002/2013GL056756

Pawlowicz, R., Beardsley, B., & Lentz, S. (2002). Classical tidal harmonic analysis including error estimates in MATLAB using T_TIDE. *Computers & Geosciences*, *28*(8), 929–937. https://doi.org/10.1016/S0098-3004(02)00013-4

Rosman, J. H., Koseff, J. R., Monismith, S. G., & Grover, J. (2007). A field investigation into the effects of a kelp forest (Macrocystis pyrifera) on coastal hydrodynamics and transport. *Journal of Geophysical Research*, *112*, C02016. https://doi.org/10.1029/2005JC003430

Selker, J. S., Thévenaz, L., Huwald, H., Mallet, A., Luxemburg, W., van de Giesen, N., et al. (2006). Distributed fiber-optic temperature sensing for hydrologic systems. *Water Resources Research*, *42*, W12202. https://doi.org/10.1029/2006WR005326

Shearman, R. K., & Lentz, S. J. (2004). Observations of tidal variability on the New England shelf. *Journal of Geophysical Research*, *109*, C06010. https://doi.org/10.1029/2003JC001972

Shroyer, E. L., Moum, J. N., & Nash, J. D. (2009). Observations of polarity reversal in shoaling nonlinear internal waves. *Journal of Physical Oceanography*, *39*, 691–701. https://doi.org/10.1175/2008JPO3953.1

Simpson, J. H., & Hunter, J. R. (1974). Fronts in the Irish Sea. *Nature*, *250*(5465), 404–406.

Sinnett, G., Feddersen, F., Lucas, A. J., Pawlak, G., & Terrill, E. (2018). Observations of nonlinear internal wave run-up to the surfzone. *Journal of Physical Oceanography*, *48*, 531–554. https://doi.org/10.1175/jpo-d-17-0210.1

Suárez, F., Aravena, J. E., Hausner, M. B., Childress, A. E., & Tyler, S. W. (2011). Assessment of a vertical high-resolution distributed-temperature-sensing system in a shallow thermohaline environment. *Hydrology and Earth System Sciences*, *15*, 1081–1093. https://doi.org/10.5194/hess-15-1081-2011

Thomas, J. A., Lerczak, J. A., & Moum, J. N. (2016). Horizontal variability of high-frequency nonlinear internal waves in Massachusetts Bay detected by an array of seafloor pressure sensors. *Journal of Geophysical Research: Oceans*, *121*, 5587–5607. https://doi.org/10.1002/2016JC011866

Thorpe, S. A., & Lemmin, U. (1999). Internal waves and temperature fronts on slopes. *Annales Geophysicae*, *17*, 1227–1234. https://doi.org/10.1007/s00585-999-1227-6

Tilburg, C. E., & Garvine, R. W. (2003). Three-dimensional flow in a shallow coastal upwelling zone: Alongshore convergence and divergence on the New Jersey shelf. *Journal of Physical Oceanography*, *33*(10), 2113–2125. https://doi.org/10.1175/1520-0485(2003)033%3C2113:TFIASC%3E2.0.CO;2

Tyler, S. W., Selke, J. S., Hausner, M. B., Hausner, C. E., Torgersen, T., Thodal, C. E., & Schladow, S. G. (2009). Environmental temperature sensing using Raman spectra DTS fiber-optic methods. *Water Resources Research*, *45*, W00D23. https://doi.org/10.1029/2008WR007052

van de Giesen, N., Steele-Dunne, S. C., Jansen, J., Hoes, O., Hausner, M. B., Tyler, S., & Selker, J. (2012). Double-ended calibration of fiber-optic Raman spectra distributed temperature sensing data. *Sensors*, *12*, 5471–5485. https://doi.org/10.3390/s120505471

Venayagamoorthy, S. K., & Fringer, O. B. (2007). On the formation and propagation of nonlinear internal boluses across a shelf break. *Journal of Fluid Mechanics*, *577*, 137–159. https://doi.org/10.1017/S0022112007004624

Walter, R. K., & Phelan, P. J. (2016). Internal bore seasonality and tidal pumping of subthermocline waters at the head of the Monterey submarine canyon. *Continental Shelf Research*, *116*, 42–53. https://doi.org/10.1016/j.csr.2016.01.015

Walter, R. K., Woodson, C. B., Leary, P. R., & Monismith, S. G. (2014). Connecting wind-driven upwelling and offshore stratification to nearshore internal bores and oxygen variability. *Journal of Geophysical Research: Oceans*, *119*, 3517–3534. https://doi.org/10.1002/2014JC009998

White, B. L., & Helfrich, K. R. (2008). Gravity currents and internal waves in a stratified fluid. *Journal of Fluid Mechanics*, *616*, 327–356. https://doi.org/10.1017/S0022112008003984

Wilkin, J. L. (2006). The summertime heat budget and circulation of southeast New England shelf waters. *Journal of Physical Oceanography*, *36*, 1997–2011. https://doi.org/10.1175/JPO2968.1

Woodson, C. (2018). The fate and impact of internal waves in nearshore ecosystems. *Annual Review of Marine Science*, *10*(1), 421–441. https://doi.org/10.1146/annurev-marine-121916-063619